Nano Research

Open Access

Research Article

Rapid preparation of graphene-skinned alumina fiber fabric and its electromagnetic interference shielding application

Kangyi Zheng[1,2], Chaojie Yu[2,3], Wenjuan Li[2,4], Fushun liang[2,5], Longfei Liu[2,6], Ruojuan Liu[4], Hao Yuan[4], Yuyao Yang[2,4], Fan Yang[2,5], Shuting Cheng[7], Wenjing Jiang[2,8], Qingxu Su[2,4], Mengxiong Liu[2,4], Yulin Han[2,6], Xiaobai Wang[2,8] ✉, Xiaoli Sun[2] ✉, Yue Qi[2] ✉, and Zhongfan Liu[2,4] ✉

[1] *College of Energy, Soochow Institute for Energy and Materials Innovations (SIEMIS), Jiangsu Provincial Key Laboratory for Advanced Carbon Materials and Wearable Energy Technologies, Soochow University, Suzhou 215006, China*
[2] *Beijing Graphene Institute (BGI), Beijing 100095, China*
[3] *School of Physics and Electronics, Shandong Normal University, Jinan 250014, China*
[4] *Centre for Nanochemistry, Beijing Science and Engineering Centre for Nanocarbons, Beijing National Laboratory for Molecular Sciences College of Chemistry and Molecular Engineering, Peking University, Beijing 100871, China*
[5] *Academy for Advanced Interdisciplinary Studies, Peking University, Beijing 100871, China*
[6] *Academy for Advanced Interdisciplinary Research, North University of China, Taiyuan 030051, China*
[7] *School of Population and Health, Renmin University of China, Beijing 100872, China*
[8] *Department of Chemistry, School of Light Industry Science and Engineering, Beijing Technology and Business University, Beijing 100048, China*

Cite this article: *Nano Research*, **2025**, *18*, 94907330. https://doi.org/10.26599/NR.2025.94907330

ABSTRACT: Direct growth of graphene on dielectric or insulating materials via chemical vapor deposition (CVD) offers a novel, transfer-free approach for various applications. However, challenges remain in growing graphene on non-catalytic substrates. In particular, the low growth rate of graphene remains a significant barrier to its large-scale production. In this study, propane (C_3H_8) was used as the carbon source to prepare graphene on commercial alumina fiber fabric (AFF) via CVD, resulting in the synthesis of a novel material: graphene-skinned alumina fiber fabric (GAFF). Through comparative analysis of the graphene growth behaviors using C_3H_8 and traditional carbon sources (CH_4 and C_2H_4) on AFF, the growth mechanism of C_3H_8 was elucidated. The pyrolysis of C_3H_8 generates the unique carbon species C_3H, which exhibits distinct advantages in terms of migration, nucleation, and growth on AFF. Graphene nucleation density using C_3H_8 was found to be 160 times higher than that of CH_4 and 50 times higher than C_2H_4. The resulting GAFF exhibits a wide tunable electrical conductivity range (1 to 7000 Ω·sq^{-1}), high tensile strength (> 170 MPa), lightweight properties, flexibility, and a hierarchical macrostructure. These characteristics make GAFF a promising candidate for various applications, including electromagnetic interference (EMI) shielding.

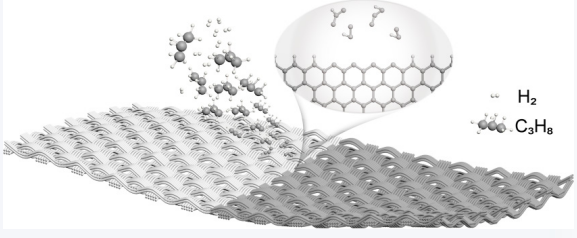

KEYWORDS: chemical vapor deposition (CVD), graphene-skinned alumina fiber fabric (GAFF), propane, electromagnetic interference (EMI) shielding

1 Instruction

The growth of graphene by chemical vapor deposition (CVD) is mainly based on the principles of metal surface catalysis and high-temperature dissolution and low-temperature precipitation of carbon sources on the metal surface, to achieve large-scale and high-quality graphene preparation [1–6]. However, during application, it needs to be transferred to the target substrate (usually dielectric/insulated), and this transfer process will inevitably lead to problems such as wrinkling, damage, and contamination of graphene, resulting in deterioration of its performance [7–12]. Growing graphene directly on the target dielectric/insulating substrate for subsequent transfer-free application strategies is becoming an increasingly interesting research direction [8].

However, there are some problems with preparing graphene on

Received: November 21, 2024; **Revised:** January 17, 2025
Accepted: February 24, 2025

✉Address correspondence to Zhongfan Liu, zfliu@pku.edu.cn; Yue Qi, qiyue@bgi-graphene.com; Xiaoli Sun, sunxl@bgi-graphene.com; Xiaobai Wang, wangxb@bgi-graphene.com

insulating substrates, such as a slow growth rate and small graphene domain size on non-catalytic substrates, due to the inertness of the surface of insulating substrates and the high migration barrier of carbon substances on their surfaces [13–17]. Therefore, exploring the rapid growth of graphene films on non-catalytic substrates is undoubtedly a great technical challenge [18–20].

Additionally, the weak pyrolysis capability of traditional carbon precursors and the absence of catalytic activity from metal atoms result in prolonged growth times for graphene on non-catalytic substrates, hindering large-scale production and industrial applications [14, 21–23]. Thus, identifying a carbon source that facilitates the rapid preparation of graphene on non-catalytic substrates is crucial for enabling its widespread application [7, 8, 24–27].

In this study, we present a novel method for synthesizing graphene utilizing propane (C_3H_8) as a carbon source, enabling the rapid and uniform deposition of graphene on alumina fiber/alumina fiber fabric (AF/AFF). A comparative analysis of methane (CH_4) and ethylene (C_2H_4), traditional carbon sources, reveals the superior growth rate associated with the C_3H_8 approach from both macro and micro perspectives. To elucidate the mechanism underlying the rapid formation of graphene facilitated by C_3H_8 molecules on AF/AFF, we employed density functional theory (DFT) to analyze the cleavage, migration, and edge splicing energy barriers of C_3H_8 and traditional carbon sources C_2H_4 and CH_4. Notably, C_3H_8 exhibits distinct advantages in terms of migration, nucleation, and growth characteristics on AFF substrates when compared to CH_4 and C_2H_4. The graphene-skinned imparts exceptional electrical and thermal conductivity properties to the graphene-skinned alumina fiber fabric (GAFF) while maintaining robust mechanical strength and high thermal stability endowed by AFF. Consequently, GAFF demonstrates promising application potential across various domains, including electromagnetic interference (EMI) shielding.

2 Experimental

2.1 Commercial AFF pretreatment process

AFF (3025t) used for graphene CVD growth was purchased from Shanghai Rongrong New Materials Company, China. Before graphene growth, commercial AFF was loaded into a quartz tube (inner diameter, 6.0 inch) within a three-zone furnace (Lindberg/Blue M Three-Zone Solid Tube Furnaces, Thermo Scientific, USA). The furnace was heated to approximately 800 °C, and air was introduced for around 2 h to eliminate surface polymers.

2.2 CVD growth of graphene on AF and AFF

During the graphene CVD growth process, a consistent flow of 100 sccm of argon (Ar) and 100 sccm of hydrogen (H_2) was introduced into the chamber during the heating stage and maintained throughout the entire CVD procedure. Once the chamber reached the target temperature (approximately 800, 900, 1000, or 1100 °C), a controlled flow of 0 to 1000 sccm of C_3H_8 (the gas mixture consists of Ar:C_3H_8 = 9:1), 0 to 100 sccm of C_2H_4, 0 to 200 sccm of CH_4, and 0 to 1000 sccm of H_2 was introduced into the CVD chamber until the graphene growth was completed, typically lasting around 250 min. Afterward, the carbon sources were halted, and the heating was turned off. The chamber was then allowed to cool, with only 100 sccm of Ar and 100 sccm of H_2 maintained during the cooling process. When the furnace chamber reached room temperature, the flow of Ar and H_2 was stopped, and the sample was extracted.

2.3 Transfer process for graphene thickness measurement

GAFF was cut into small fibers and immersed in a 50% hydrofluoric acid (HF) solution for 8 to 12 h to remove the AF core. Subsequently, the collapsed graphene ribbons coated on the fibers were thoroughly washed 3 to 5 times with deionized water to remove residual HF solution and inorganic salts from the graphene surface. Finally, the graphene ribbons were transferred onto a silicon wafer or transmission electron microscope (TEM) grid and dried under an infrared lamp for 15 to 25 min until all residual hydrofluoric acid had completely evaporated. The resulting samples can be used to measure the graphene thickness and assess its crystalline quality.

2.4 Graphene domain regions data collection and analysis methods

The graphene domain regions were collected by repeating the CVD experiments three times points of ~ 3.5, ~ 4.5, ~ 5, ~ 5.5, ~ 6, ~ 8, ~ 85, ~ 95, ~ 105, ~ 115, ~ 125, ~ 135, ~ 140, ~ 150, ~ 170, ~ 190, ~ 200, and 210 min using C_3H_8, C_2H_4, and CH_4 carbon sources. Scanning electron microscopy (SEM) characterized their surface morphology. Nucleation density and domain size were analyzed using SEM, while graphene coverage was estimated by analyzing statistical pixel values in Photoshop.

2.5 Sheet resistance of GAFF

An average of 400 samples were collected at regular intervals on the surface of GAFF, and a four-point probe resistivity measurement was employed to assess the sheet resistance of GAFF films.

2.6 Mechanical testing of GAFF

Three GAFF samples, each measuring 25 mm × 250 mm, were randomly selected. Each specimen was placed at least 100 mm from the edge, and the number of contacts should be minimized. The instrument (YG207A) moved the steel ruler and specimen forward at a controlled speed, causing the specimen to penetrate the leading edge of the platform and bend under its weight until the deep end was recorded as D. The experiment was repeated three times at the opposite end and on the other side of the GAFF. When the test tip reaches an inclined plane at a 41.5° angle to the horizontal at the leading edge of the platform, the protruding length is twice the test bending length, from which the bending length is determined. Half of the protruding length is taken as the bending length. Four bending lengths were recorded for each sample, and the average bending length (C) was calculated for each specimen. The flexural stiffness (G) is calculated using the equation (Eq. (1)):

$$G = m \times C^3 \times 10^{-3} \quad (1)$$

where G is the flexural stiffness (mN·cm), m is the mass per unit area of the sample (g·m^{-2}), and C is the average bending length of the specimen (cm). The test method is derived from GB/T 18318.1-2009.

To ensure accurate data collection during fabric testing, attach A4 paper (10 mm × 10 mm) to both ends of the GAFF sample to prevent slippage and data inaccuracies. Both ends of the GAFF

sample were secured to an electronic universal materials testing machine (MTS E43.104) using grippers, along with the attached A4 paper. Ensure the longitudinal centerline of the specimen remains aligned. The distance between the two grippers was set to 200 mm, with the gripper ends positioned approximately 10 mm from the GAFF specimen (≥ 220 mm). The GAFF specimen was continuously stretched at a rate of 100 mm/10 min. The instantaneous tensile force (F) was recorded when the tensile force reached the point of failure. The maximum tensile strength (σ) was calculated based on the peak stress (F) observed before the fiber bundle failed, as follows (Eq. (2))

$$\sigma = \frac{F}{b} \tag{2}$$

where σ is the tensile strength (GPa), F is the breaking load (N), and b is the cross-sectional area of the GAFF bundle (cm²). The cross-section of GAFF is averaged by measuring 20 points with altitude gages. The test method is derived from GB/T 3923.1-2013.

2.7 Electromagnetic shielding of GAFF

GAFF samples, with dimensions of at least 30 mm × 30 mm, were secured in place using an X-band test fixture (DR-WX) via the waveguide method. Testing was performed using a vector network analyzer (Keysight E5063A).

2.8 Measurement for the thickness of graphene layers in GAFF

To measure the thickness of graphene layers grown on AF, the AF core in graphene-skinned alumina fiber (GAF) obtained from GAFF was etched away in HF (see more details in the method (Section 2.3)), transfer process for graphene thickness measurement). After etching AF in GAF, graphene layers on the fiber substrate collapsed onto the silicon wafer forming the graphene ribbons. The height of graphene ribbons can be measured using atomic force microscopy (AFM) and the prepared graphene's thickness can be calculated using Eq. (3) [28]

$$h_0 = \frac{(h - 0.4 \times 2)}{2}\,(\text{nm}) \tag{3}$$

where h_0 and h are the thickness of graphene layers and the average height of graphene ribbons measured with AFM, respectively. 0.4 × 2 value the correction accounting for the measured thickness increase related to substrate-graphene and graphene-tip interactions, as well as the interlayer interaction of graphene.

2.9 Characterizations

GAFF samples were characterized using SEM (FEI Quattro S, 10 kV), Raman spectroscopy (Horiba, LabRAM HR-800, 532 nm laser excitation), and AFM (Bruker Dimension Icon, tapping mode). Sheet resistance was measured using a four-point probe resistivity system (RTS-8), while electrical conductivity was assessed using a Keithley 2400 (Tektronix). Tensile testing, including the determination of bending behavior, was performed using the incline method. Bending rigidity was evaluated using the inclined plane method, with each test sample measuring 25 mm × 250 mm (YG207A). The tensile strength of the GAFF samples was evaluated using an electronic universal material testing machine (MTS E43.104). Electromagnetic shielding was evaluated using vector network analysis (E5063A) with the Waveguide Test Fixture (DR-WX) and associated software (DR-WSE).

2.10 DFT computational details

All the calculations were performed by using DFT as implemented in the Vienna *ab initio* package (VASP) [29]. The projector augmented wave (PAW) method [30] was used to describe electron-ion interaction, while the generalized gradient approximation using the Perdew–Burke–Ernzerhof (PBE) function was used to describe the electron exchange correlation. A plane wave basis was set up to an energy cutoff of 400 eV. For structural optimizations and charge density calculations, the convergence criterion for the total energy was set to 1×10^{-4} eV, and that of the force on each atom was set to 0.02 eV·Å^{-1}. Monkhorst–Pack scheme k-point grids of 1 × 1 × 1 were used, and the transition states were searched using the climbing-image nudged elastic-band (CI-NEB) method integrated into VASP. Two layers of metal atoms and one layer of oxygen atoms for one cycle repeated four cycles as the substrate in the model for the γ-Al_2O_3 graphene coverage models, and the bottom two layers were fixed to imitate the surface's relaxation state. The graphene edge consists of nanoribbons covering the surface of Al_2O_3. A correction was performed using the DFT-D3 method, considering the van der Waals force correction [31].

3 Results and discussion

In this work, C_3H_8 was utilized for graphene growth on AFF to realize the conformal coverage of continuous graphene layers on each fiber via the CVD method (Fig. 1(a)). The component content of commercial AF is Al_2O_3:SiO_2 = 72%:28%. It is worth noting that the microstructure and composition of AF remain unchanged after heat treatment at 1100 °C for 2 h (Fig. S1(a) in the ESM), which enables high-temperature graphene growth. Figure 1(b) compares images of the photographs before and after the preparation of GAFF via CVD by AFF. The Raman spectra presented in Fig. 1(c) were obtained from eight evenly spaced locations on the GAFF, as shown in Fig. 1(b). The uniformity of the intensity I_D/I_G (the intensity ratio of the D and G peaks) and I_{2D}/I_G (the intensity ratio of 2D and G peaks), further confirms the excellent homogeneity of graphene on the fiber surface.

Moreover, the conformal coverage observed in SEM images (Fig. 1(d)) and uniform Raman 2D peak mapping (Fig. 1(e)) confirm the continuous, uniform graphene layer coverage. Raman mapping of GAF was obtained using single-point Raman spectroscopy (30 × 50). The number of graphene layers can be effectively controlled, allowing the synthesis of GAFF with varying graphene thicknesses (Fig. 1(f)). Raman spectroscopy further demonstrates that the controlled preparation of GAFF can be achieved by adjusting the C_3H_8 and H_2 gas flow rates (Fig. 1(g)). GAFF thickness can be measured using AFM with different C_3H_8/H_2 gas flow ratios. The actual graphene thickness can also be determined by HF etching AF and transferring the graphene strip to a silicon wafer (Fig. S2 in the ESM) (the transfer process is detailed in Section 2.3). The few-layer GAFF shown in Fig. 1(f) was further characterized using high-resolution transmission electron microscopy (HR-TEM) (Fig. 1(h)), revealing stacked layers of few-layer graphene. Additionally, the selected area electron diffraction (SAED) pattern in the inset of Fig. 1(h) indicates the high crystalline quality of graphene.

Meanwhile, under identical experimental conditions, the experiment was repeated to generate different batches of GAFF (Fig. S3(a) in the ESM), with Raman spectra collected from three uniformly spaced positions, as shown in Fig. S2(a) in the ESM (Fig.

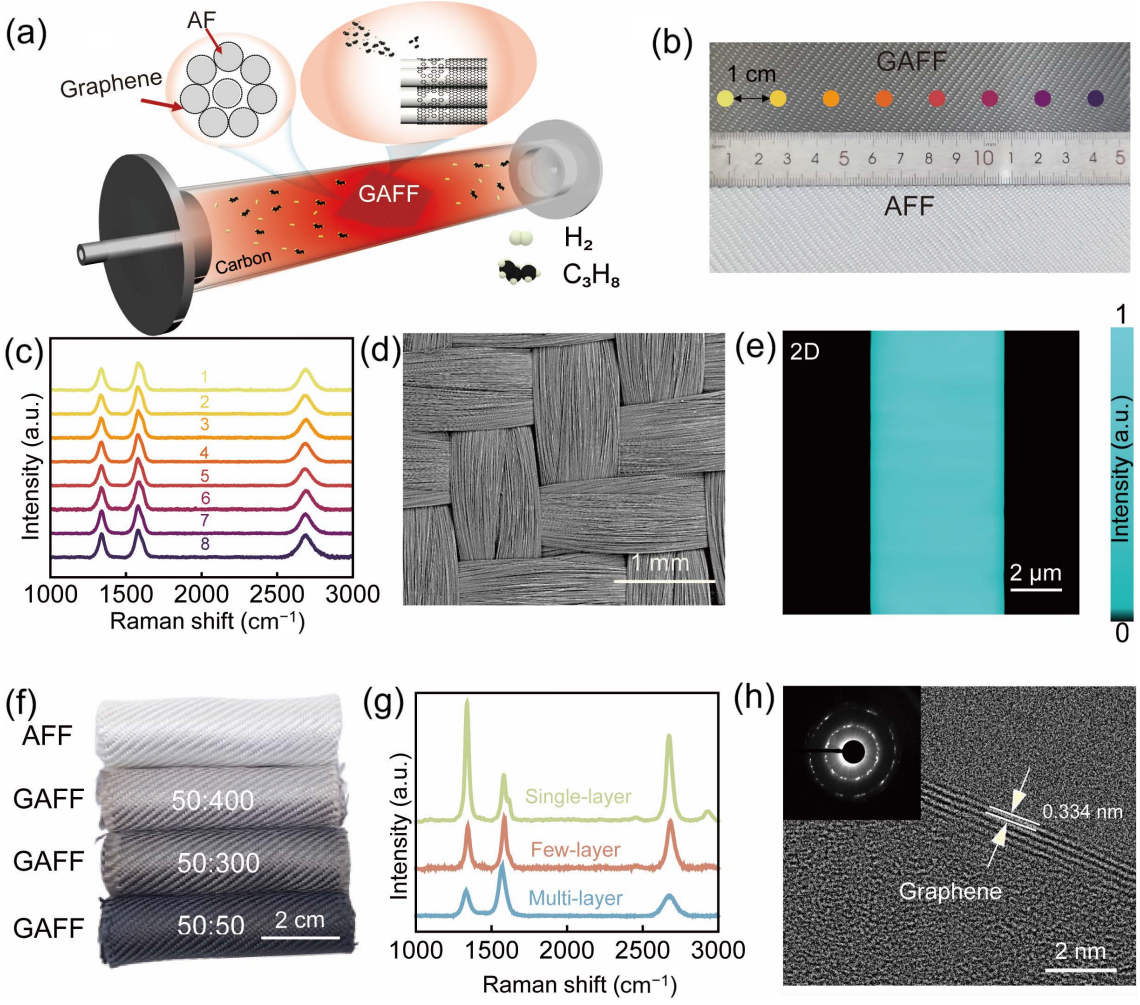

Figure 1 Preparation and characterization of GAFF by CVD with carbon source of C_3H_8. (a) The schematic diagram of GAFF prepared by CVD with C_3H_8 as the carbon source. (b) Photographs of AFF (bottom) and GAFF (upper). (c) Raman spectra obtained from 8 evenly-spaced positions on GAFF, as marked in (b). (d) SEM image of GAFF with twill, scale bar: 1 mm. (e) Raman spectrum mapping of GAF in (b), scale bar: 2 μm. (f) Photographs of AFF and GAFFs prepared with different C_3H_8/H_2 ratios, scale bar: 2 cm. (g) Raman spectra of GAFF with single-layer, few-layer, and multi-layer graphene in (f), few-layer and multi-layer graphene are 4 and 224 layers, respectively. (h) HR-TEM image of 5-layer graphene and corresponding SAED patterns in the inset, with a scale bar of 10 nm.

S3(b) in the ESM). The resulting spectra exhibited consistent I_D/I_G and I_{2D}/I_G ratios, confirming the stability and reproducibility of GAFF preparation using C_3H_8 as the carbon source.

To further investigate the rapid growth behavior of C_3H_8, we compared it with two traditional carbon sources, C_2H_4 and CH_4, by analyzing their growth behaviors through SEM images. The reasons for C_3H_8's accelerated growth were explored from both micro and macro perspectives. In the experiment, the gas flow rates were controlled to ensure consistent carbon atomic numbers across all sources (C_3H_8:C_2H_4:CH_4 = 2:3:6), thereby eliminating the influence of differing carbon atomic numbers.

This is shown in (Figs. S4(a)–S4(c) in the ESM). SEM images show that multiple graphene domain regions were formed on the surface of GAFF at 6 min for the C_3H_8 carbon source. The graphene domain regions of the CH_4 and C_2H_4 carbon sources grew slowly after ~ 85 and ~ 140 min, and at ~ 210 and ~135 min, the graphene domain regions had similar coverage to the graphene domain regions formed by the C_3H_8 carbon source at 8 min.

This indicates that the C_3H_8 carbon source has a shorter incubation time for graphene preparation on the AFF surface, which allows for faster preparation of GAFF. Figure 2(c) shows the nucleation density of graphene prepared from C_3H_8, C_2H_4, and CH_4 carbon sources as a function of time, with a linear increase. The nucleation time ($^*t_0$) can be calculated by linear fitting extrapolation, as shown by the pentagon asterisk in Fig. 2(c). The nucleation time of graphene with CH_4, C_2H_4, and C_3H_8 as carbon sources was ~ 110, ~ 48, and ~ 2 min, respectively. The results indicate that the nucleation speed of the C_3H_8 carbon source method is significantly faster. The nucleation rate of graphene prepared from the C_3H_8 carbon source (~ 37.17 nuclei·μm^{-2}·min^{-1}) was significantly higher than that of the C_2H_4 carbon source (~ 0.73 nuclei·μm^{-2}·min^{-1}) and CH_4 carbon source (~ 0.23 nuclei·μm^{-2}·min^{-1}). Figure 2(d) shows the graphene domain sizes as a function of growth time, where the slope represents the growth rate of domain sizes. The growth rate of the C_3H_8 carbon source method (~ 13.31 nm·min^{-1}) was much greater than that of the graphene domain regions prepared by the CH_4 carbon source (~ 0.97 nm·min^{-1}) and C_2H_4 carbon source (~ 1.40 nm·min^{-1}). From the linear fit extrapolation calculation in Fig. 2(d), it can be observed that the $^*t_0$ obtained in Fig. 2(d) is in good agreement with the $^*t_0$ obtained in Fig. 2(c). The nucleation rate and growth rate of graphene domain regions prepared by the

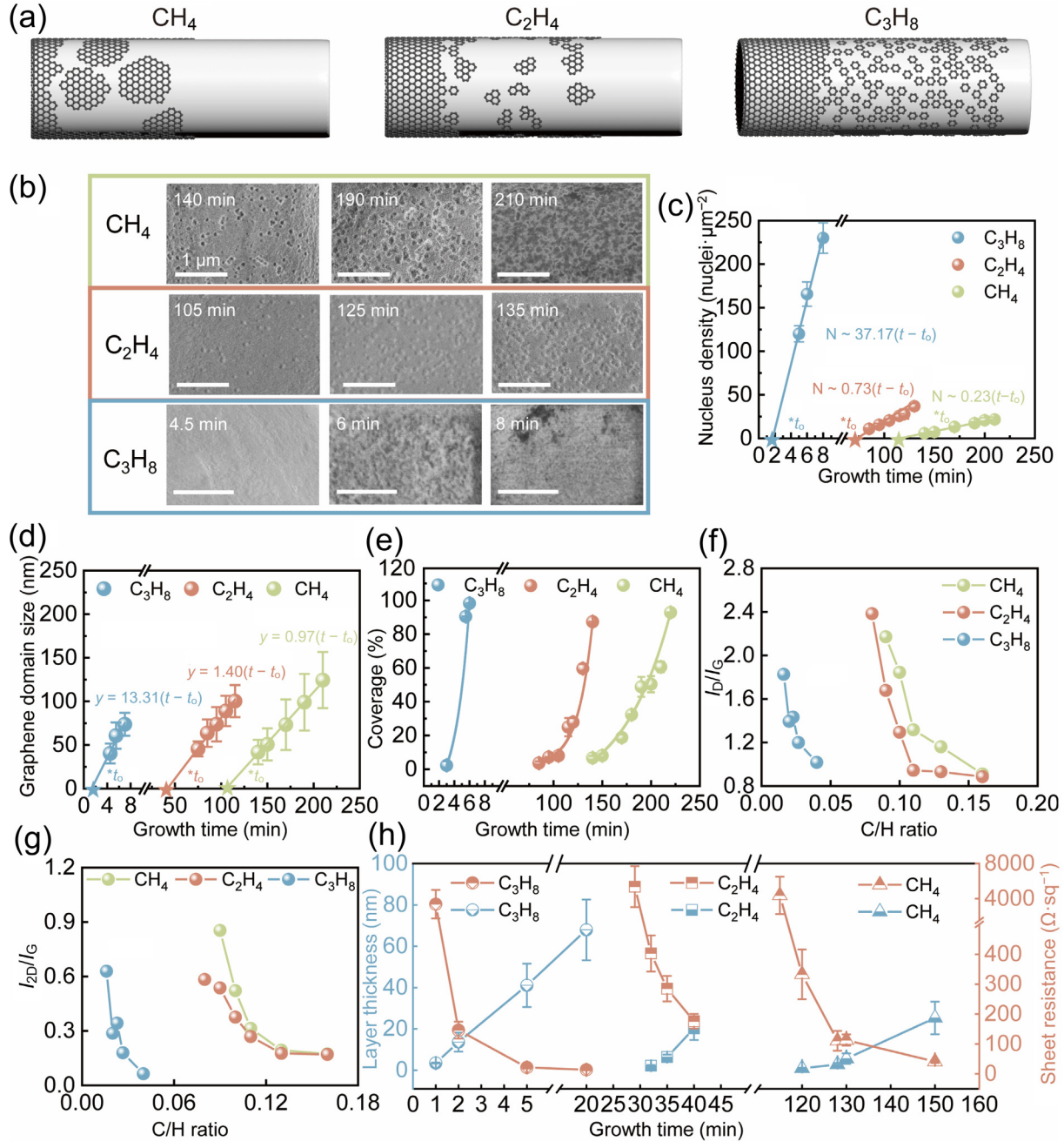

Figure 2 Comparison of the graphene growth behavior of C_3H_8, CH_4, and C_2H_4 carbon sources. (a) A schematic diagram of GAF prepared using CH_4, C_2H_4, and C_3H_8 respectively. (b) SEM images of the graphene domain regions on AF with three carbon sources of CH_4, C_2H_4, and C_3H_8 under different coverages, scale bar: 1 μm. (c) Nucleation densities of graphene domain regions on AF with three carbon sources of CH_4, C_2H_4, and C_3H_8 at different growth times. The nucleation time $*t_0$ time of C_3H_8, C_2H_4, and CH_4 was 2, 48, and 110 min, respectively. (d) Graphene island domain sizes on AF with three carbon sources of CH_4, C_2H_4, and C_3H_8 with various growth times. The nucleation time $*t_0$ time of C_3H_8, C_2H_4, and CH_4 was 2, 48, and 110 min, respectively. (e) The coverage change of graphene domain regions on AF as a function of growth time with CH_4, C_2H_4, and C_3H_8. The error bars represent the standard deviations (n = 3). (f) and (g) The I_D/I_G and I_{2D}/I_G of graphene prepared by CH_4, C_2H_4, and C_3H_8 carbon sources at different C/H ratios. (h) The sheet resistance and layer thickness of GAFF prepared with CH_4, C_2H_4, and C_3H_8 with various growth times.

C_3H_8 carbon source were significantly higher than those of graphene prepared from CH_4 and C_2H_4 carbon sources, to achieve faster full coverage. With the extension of the reaction time, the graphene domain regions gradually aggregate to form a continuous graphene film, and finally completely cover the AF surface. The nucleation density of graphene (Fig. 2(b)) and graphene domain size (Fig. 2(c)) indicate that graphene prepared from the C_3H_8 carbon source has a high domain density and a smaller domain size. In contrast, graphene prepared from the CH_4 carbon source has a small domain density and a larger domain size. It is worth noting that graphene prepared from the C_3H_8 carbon source can achieve near-complete coverage at ~ 8 min, while CH_4 and C_2H_4 can achieve similar coverage after ~ 210 and ~ 135 min (Fig. 2(d)), which is consistent with the fast growth rate of graphene prepared from the C_3H_8 carbon source mentioned earlier. From a macro point of view, the C_3H_8 carbon source requires the smallest C/H ratio at similar I_D/I_G and I_{2D}/I_G (Figs. 2(f) and 2(g)). The C_3H_8 carbon source takes the least time to prepare GAFF under similar

graphene thickness and sheet resistance (Fig. 2(h)). The actual thickness of the graphene is obtained from AFM images (Figs. S5–S7 in the ESM), and the transfer process is detailed in the method.

The rapid, homogeneous, and large-scale preparation of GAFF is essential for its practical applications. Graphene film preparation via CVD is a kinetic process in which carbon sources and precursors are transported to the substrate surface, following the direction of the gas flow. On the surface of γ-Al_2O_3, which acts as a Lewis acid catalyst [8, 32–35], active species overcome the adsorption energy barrier of the substrate. These species are then randomly deposited onto the substrate surface, significantly reducing the precursor incubation time on the AFF surface. As the number of graphene attachment sites increases, the precursors tend to undergo secondary growth at these sites, leading to the formation of graphene domain regions. During the graphene preparation process, edge carbon atoms attached to graphene sites are more likely to escape into the surrounding environment [36].

In this study, the DFT method was employed to investigate the molecular properties of C_3H_8 and its role in the fundamental process of graphene CVD growth. Key steps in the graphene CVD growth process were analyzed, including the cleavage of carbon precursors (Fig. S8 in the ESM), the migration and nucleation of active species, and the energy barriers associated with edge growth, as illustrated in Fig. 3.

On AF substrates, the C_2H barrier (6.78 eV) and C_3H barrier (6.18 eV), the primary active carbon species cleaved by C_3H_8 carbon source, are higher than those of CH_3 (4.24 eV), the primary active carbon species cleaved by CH_4 carbon source, and the C_2H band (4.29 eV), the primary active carbon species cleaved by C_2H_4 carbon source (Fig. 3(a)). The migration barrier of the carbon active species C_3H (3.46 eV) to C_3H_8 was lower than that of the activated carbon species CH_3 (5.16 eV) of the CH_4 carbon source and much less than that of the shared activated carbon species C_2H (7.34 eV) of the C_3H_8 and C_2H_4 carbon sources (Fig. 3(b)). Notably, Fig. 3(c) underscores the significant superiority of the primary carbon species C_3H derived from C_3H_8 in terms of nucleation rates, suggesting that the C_3H_8 carbon source can migrate and nucleate rapidly, resulting in a significant enhancement of growth, which is consistent with previous experimental data. Figure 3(d) shows that the splicing energy barrier of C_3H_8-derived primary carbon species C_3H is lower than that of C_2H, a primary carbon species shared by C_3H_8 and C_2H_4, indicating that the C_3H_8 carbon source has a faster growth rate in the domain regions.

In practical application, high flexibility and electrical conductivity are the significant advantages of GAFF [37]. The AFF was coated with graphene by CVD, and a large area (200 cm × 50 cm) of uniform GAFF was prepared (Fig. 4(a)), giving the commercial AFF exceptional mechanical and electrical properties. Figure 4(b) shows the corresponding film sheet resistance uniformity of GAFF in Fig. 4(a). The graphene-coated is uniformly distributed on the surface of the AFF, and the average sheet resistance is 22.5 ± 3.0 Ω·sq^{-1}. At a bending radius of ~ 20 mm, the anterior and posterior resistance of the diaphragm did not change much after different bending times (Fig. 4(c)), indicating that there is a strong binding force between graphene and the AF coating, and graphene is not easy to fall off. It is notable that by changing the thickness of graphene, the sheet resistance of GAFF can be effectively adjusted

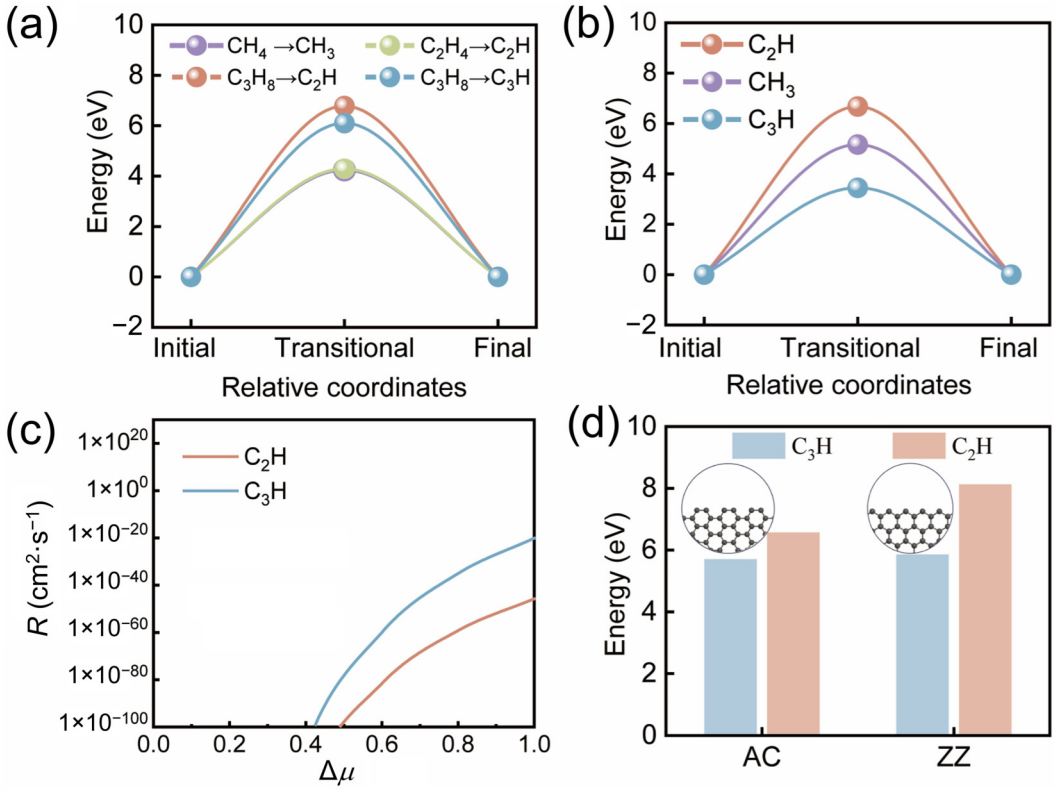

Figure 3 Comparison of CVD growth mechanisms of graphene prepared from CH_4, C_2H_4, and C_3H_8 carbon sources on γ-Al_2O_3. (a) The carbon sources of CH_4, C_2H_4, and C_3H_8 on γ-Al_2O_3 substrates are characterized by cleavable energy barriers associated with the primary active species. (b) The migration barriers of the primary active species on γ-Al_2O_3 substrates. (c) The nucleation rate of the primary active substance on the γ-Al_2O_3 (100) crystal plane. (d) The edge growth barriers of the primary active species on the γ-Al_2O_3 substrates.

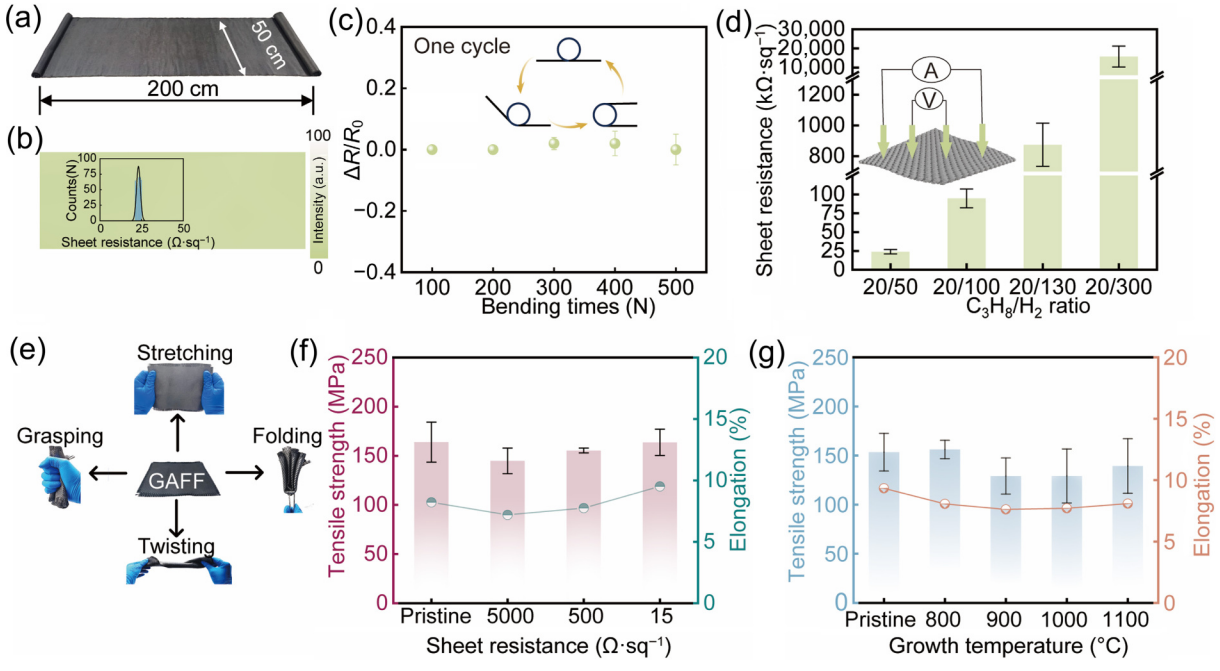

Figure 4 Electrical and mechanical properties of GAFF. (a) Photograph of GAFF (50 cm × 200 cm). (b) Sheet resistance mapping of GAFF. (c) Resistance variations of GAFF after 500 times bending at a bending radius of ≈ 20 mm. The error bars represent the standard deviations (n = 3). (d) Sheet resistance of GAFF with various C_3H_8/H_2 ratios. (e) Photographs of GAFF going through mechanical deformations of grasping, folding, twisting, and stretching. (f) The tensile strength and elongation of GAFF obtained at different graphene layers (~ 5, ~ 26, and ~ 113 N). The error bars represent the standard deviations (n = 3). (g) Tensile strength and elongation of the pristine AFF and GAFF obtained at different growth temperatures (~ 800, ~ 900, ~ 1000, and ~1100 °C for ~ 2 h). The error bars represent the standard deviations (n = 3).

in a wide range, and the thickness of graphene can be achieved by adjusting the growth parameter of the C_3H_8/H_2 ratios of graphene (Fig. 4(d)).

Moreover, GAFF exhibits excellent flexibility and retains high tensile strength even at 1100 °C. After undergoing repeated mechanical deformations, including grasping, folding, twisting, and stretching (Fig. 4(e)), the changes in the I_D/I_G and I_{2D}/I_G ratios of GAFF were negligible (Fig. S9 in the ESM).

This stability indicates that the graphene layers within GAFF maintain their structural integrity despite various mechanical stresses. The tensile strength of GAFF was assessed from two perspectives: the graphene layers of the GAFF (Fig. 4(f)) and the heat treatment temperature of the AFF (Fig. 4(g)). The number of graphene layers can be controlled by adjusting the C_3H_8/H_2 ratios, allowing for the synthesis of GAFF films with varying sheet resistances. Interestingly, the tensile strength and elongation of GAFF remained largely unaffected by changes in graphene thickness (Fig. S10 in the ESM) (the transfer process is detailed in the method). However, both the tensile strength (Fig. 4(g)) and flexural rigidity (Fig. S11 in the ESM) of the AFF were significantly reduced when the heat treatment temperature (~ 800, ~ 900, ~ 1000, and ~ 1100 °C, Ar: 500 sccm for 2 h) for graphene growth was altered.

With the rapid advancement of science and technology, particularly in areas such as 5G high-frequency communications, smart wearable devices, and new energy vehicles, the influence of electromagnetic interference (EMI) has become pervasive, impacting everything from daily life to military operations and even space exploration [38–40]. Consequently, there is a growing need to develop materials capable of shielding or absorbing electromagnetic waves to mitigate these harmful effects [38, 41–43]. Electromagnetic shielding materials are functional substances designed to reduce the transmission of electromagnetic wave (EMW) energy through absorption (A) and reflection (R), thereby effectively countering electromagnetic interference and pollution [44–47]. The effectiveness of such shielding materials depends on their conductivity, permeability, and structural design [48, 49].

As technology advances, electromagnetic shielding materials are evolving towards being lighter, thinner, and more efficient to meet the increasing market demand [50]. In recent years, graphene has emerged as a key carbon material in the field of nanotechnology, known for its exceptional electron mobility, high thermal stability, and large specific surface area [51, 52]. The GAFF, synthesized via the CVD method by integrating graphene with AFF, has demonstrated significant improvements in both the electrical conductivity and electromagnetic shielding capabilities of AFF [8, 46, 53].

This paper investigates the influence of graphene thickness, fabric count, and polyimide (PI) encapsulation films on EMI shielding performance. The AFF used in this study is a twill fabric structure consisting of warp and weft yarns. The graphene composites developed possess a distinctive layered conductive structure, offering unique advantages for EMI shielding applications.

As illustrated on the left side of Fig. 5(a), from a macroscopic perspective, when EMW incident on a multilayer (1–3 layers) GAFF, most of the EMW is reflected due to its interaction with the free carriers on the graphene surface. At the microscopic level, a small portion of the EMW penetrates the braided structure of the GAFF, where it undergoes multiple reflections between adjacent fibers, coupled with successive absorptions. The magnified image on the right side of Fig. 5(a) demonstrates that when EMW interacts with a single GAF in the fabric, part of the EMW is reflected by the graphene layer, while the remainder is absorbed due to the

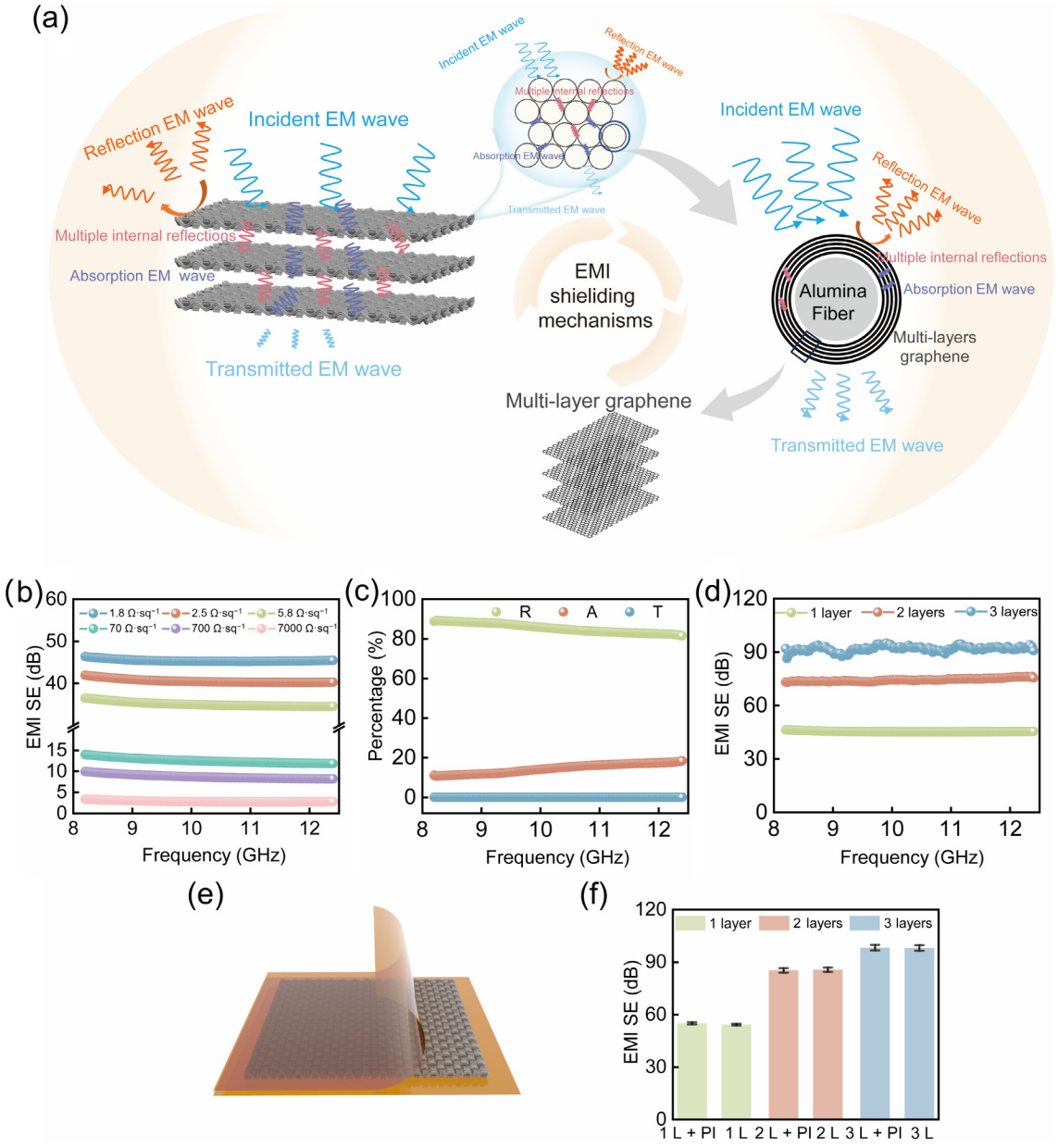

Figure 5 Electromagnetic properties of GAFF. (a) EMI shielding mechanisms in the hierarchical conducive configuration of GAFF. (b) The EMI shielding effectiveness (SE) of GAFFs with different sheet resistances (1.8, 2.5, 5.8, 70, 700, and 7000 Ω·sq^{-1}). (c) Reflection (R), absorption (A), and transmission (T) ratio of GAFF with a sheet resistance of 1.8 Ω·sq^{-1}. (d) EMI SE of the 1–3 layers of GAFFs (thickness of GAFF to ~ 0.40 mm, sheet resistance of ~ 1.8 Ω·sq^{-1}). (e) A schematic diagram of encapsulation of GAFF with polyimide (PI) film. (f) EMI SE of GAFF before and after packaging by PI. The error bars represent the standard deviations (n = 3).

conductive losses, and polarization relaxation in the graphene layer. Notably, the electromagnetic interference shielding effectiveness (EMI SE) of GAFF can be effectively tuned by adjusting the number of graphene layers, which can be controlled by varying the growth time. For instance, at a sheet resistance of 1.8 Ω·sq^{-1}, the EMI SE reaches approximately 46 dB (Fig. 5(b)). EMI SE and dielectric constant of AFF (Fig. S12 in the ESM). Sub-tests of GAFF with this resistance demonstrated that 90% of the EMW was reflected, with less than 1% transmitted, confirming the effective electromagnetic shielding performance of GAFF (Fig. 5(c)). To further enhance shielding efficiency, multilayer GAFF was fabricated, and its EMI SE showed an increasing trend. The EMI SE of the multilayer GAFF reached around 90 dB (Fig. 5(d)). The impedance matching and attenuation coefficient of GAFF (Fig. S13 in the ESM). Comparison of the specific shielding effectiveness of GAFF with other shielding materials (Fig. S14 in the ESM).

The PI film is renowned for its outstanding resistance to both high and low temperatures, excellent mechanical properties, chemical stability, favorable dielectric characteristics, and biocompatibility. These qualities make it highly versatile and widely used in applications such as microelectronic packaging, new energy batteries, and chemical equipment [54–57]. In addition, PI film significantly enhances the mechanical strength of GAFF, improves its thermal stability, and boosts its electrical insulation, offering effective protection for GAFF against external environmental factors [58–60].

The encapsulation of PI and GAFF is achieved by layering PI over GAFF within a thermoplastic molding machine. It is crucial to

preserve the integrity and performance stability of the graphene both before and after encapsulation, to prevent oxidation and ensure the long-term stability of GAFF's electromagnetic shielding effectiveness. Figure 5(e) depicts the structural model of GAFF encapsulated with a PI film. Notably, the electromagnetic shielding efficiency of GAFF shows minimal change before and after the application of different encapsulation layers, indicating that the PI film does not impact the shielding performance (Fig. 5(f)). Additionally, Fig. S15 in the ESM presents a photo of the PI-encapsulated GAFF (20 cm × 10 cm) for reference.

4 Conclusions

In this study, C_3H_8 was employed as the carbon source to enable the rapid preparation of GAFF on an AFF substrate via the CVD method. A comparative analysis of the growth behavior of C_3H_8 versus traditional carbon sources, CH_4 and C_2H_4, revealed that C_3H_8 demonstrated superior growth rates across both microscopic (including graphene domain size, nucleation density, and coverage) and macroscopic perspectives (including defect ratio, graphene film thickness, and sheet resistance). DFT analysis identified C_2H and C_3H as the primary active species generated during the pyrolysis of C_3H_8 at 1100 °C. Notably, C_3H, as a unique active species of C_3H_8, showed distinct advantages in migration, nucleation, and growth on AFF substrates compared to traditional carbon sources. Overall, utilizing C_3H_8 as an innovative carbon source for graphene synthesis on commercial AFF substrates opens up new avenues for large-scale production and commercialization. The resulting GAFF exhibits exceptional properties such as flexibility, tensile strength, electrical conductivity, and electromagnetic shielding, providing a strong foundation for future applications. Further optimization of preparation processes and structural design will not only enhance performance but also expand the potential application areas of GAFF, positioning it for broader use in applications such as electromagnetic shielding materials.

Electronic Supplementary Material: Supplementary material (data related to the uniformity of GAFF preparation from methane, ethylene and propane carbon sources, C/H ratio, growth behavior of graphene and electromagnetic properties) is available in the online version of this article at https://doi.org/10.26599/NR.2025.94907330.

Acknowledgements

This work was financially supported by the National Natural Science Foundation of China (Nos. T2188101, 52272032, 12302236, and 52021006).

Declaration of competing interest

All the contributing authors report no conflict of interests in this work. Author Zhongfan Liu is the advisory board member of this journal, but he is not involved in the peer-review or decision of this article.

Author contribution statement

Z. F. L., Y. Q., X. L. S., X. B. W., and K. Y. Z. conceived and designed the experiments. Z. F. L., Y. Q., X. L. S., and X. B. W. supervised the project. K. Y. Z., W. J. L., F. H. L., L. F. L., R. J. L., H. Y., Y. Y. Y., F. Y., S. T. C., W. J. J., Q. X. S., M. X. L., and Y. L. H. performed the characterizations including SEM, AFM, TEM, Raman spectroscopy, and sheet resistance measurements. K. Y. Z., C. J. Y., W. J. L., F. H. L., Y. L. H., and X. L. S. investigated the mechanism underlying propane-promoted rapid preparation of GAFF. K. Y. Z., W. X. L., W. J. J., and F. H. L. conducted tests on mechanical and electromagnetic properties guided by Z. F. L., Y. Q., X. L. S., and X. B. W. K. Y. Z., F. H. L., W. J. L., Y. L.H., and W. J. J. conducted data analysis and wrote the manuscript. All authors contributed to the discussion and analysis of the results.

Use of AI statement

During the preparation of this work, the authors used Grammarly in order to language polishing. After using this tool/service, the authors reviewed and edited the content as needed and take full responsibility for the content of the publication.

References

[1] Piccinini, E.; Fenoy, G. E.; Cantillo, A. L.; Allegretto, J. A.; Scotto, J.; Piccinini, J. M.; Marmisollé, W. A.; Azzaroni, O. Biofunctionalization of graphene-based FET sensors through heterobifunctional nanoscaffolds: Technology validation toward rapid COVID-19 diagnostics and monitoring. *Adv. Mater. Interfaces* **2022**, *9*, 2102526.

[2] Nayak, P. K. Direct growth of graphene on insulator using liquid precursor via an intermediate nanostructured state carbon nanotube. *Nanoscale Res. Lett.* **2019**, *14*, 107.

[3] Pawar, S.; Duadi, H.; Fixler, D. Recent advances in the spintronic application of carbon-based nanomaterials. *Nanomaterials* **2023**, *13*, 598.

[4] Wu, D.; Wang, M. C.; Zeng, J. W.; Yao, J. Y.; Jia, C.; Zhang, H.; Li, J. T. Preparation and characterization of graphene from refined benzene extracted from low-rank coal: Based on the CVD technology. *Molecules* **2021**, *26*, 1900.

[5] Zhan, L. L.; Wang, Y.; Chang, H. C.; Stehle, R.; Xu, J.; Gao, L. B.; Zhang, W. L.; Jia, Y.; Qing, F. Z.; Li, X. S. Preparation of ultra-smooth Cu surface for high-quality graphene synthesis. *Nanoscale Res. Lett.* **2018**, *13*, 340.

[6] Kashani, H.; Ito, Y.; Han, J. H.; Liu, P.; Chen, M. W. Extraordinary tensile strength and ductility of scalable nanoporous graphene. *Sci. Adv.* **2019**, *5*, eaat6951.

[7] Wang, K.; Sun, X. C.; Cheng, S. T.; Cheng, Y.; Huang, K. W.; Liu, R. J.; Yuan, H.; Li, W. J.; Liang, F. S.; Yang, Y. Y. et al. Multispecies-coadsorption-induced rapid preparation of graphene glass fiber fabric and applications in flexible pressure sensor. *Nat. Commun.* **2024**, *15*, 5040.

[8] Li, W. J.; Liang, F. S.; Sun, X. C.; Zheng, K. Y.; Liu, R. J.; Yuan, H.; Cheng, S. T.; Wang, J. N.; Cheng, Y.; Huang, K. W. et al. Graphene-skinned alumina fiber fabricated through metalloid-catalytic graphene CVD growth on nonmetallic substrate and its mass production. *Nat. Commun.* **2024**, *15*, 6825.

[9] Grebenko, A. K.; Krasnikov, D. V.; Bubis, A. V.; Stolyarov, V. S.; Vyalikh, D. V.; Makarova, A. A.; Fedorov, A.; Aitkulova, A.; Alekseeva, A. A.; Gilshtein, E. et al. High-quality graphene using boudouard reaction. *Adv. Sci.* **2022**, *9*, 2200217.

[10] Han, Y. R.; Park, B. J.; Eom, J. H.; Jella, V.; Ippili, S.; Pammi, S. V. N.; Choi, J. S.; Ha, H.; Choi, H.; Jeon, C. et al. Direct growth of highly conductive large-area stretchable graphene. *Adv. Sci.* **2021**, *8*, 2003697.

[11] Fujita, J. I.; Hiyama, T.; Hirukawa, A.; Kondo, T.; Nakamura, J.; Ito, S. I.; Araki, R.; Ito, Y.; Takeguchi, M.; Pai, W. W. Near room temperature chemical vapor deposition of graphene with diluted methane and molten gallium catalyst. *Sci. Rep.* **2017**, *7*, 12371.

[12] Saeed, M.; Alshammari, Y.; Majeed, S. A.; Al-Nasrallah, E. Chemical

vapour deposition of graphene-synthesis, characterisation, and applications: A review. *Molecules* **2020**, *25*, 3856.
[13] Li, N.; Zhen, Z.; Zhang, R. J.; Xu, Z. H.; Zheng, Z.; He, L. M. Nucleation and growth dynamics of graphene grown by radio frequency plasma-enhanced chemical vapor deposition. *Sci. Rep.* **2021**, *11*, 6007.
[14] Zhang, Z. H.; Xu, X. Z.; Qiu, L.; Wang, S. X.; Wu, T. W.; Ding, F.; Peng, H. L.; Liu, K. H. The way towards ultrafast growth of single-crystal graphene on copper. *Adv. Sci.* **2017**, *4*, 1700087.
[15] Luceño-Sánchez, J. A.; Maties, G.; Gonzalez-Arellano, C.; Diez-Pascual, A. M. Synthesis and characterization of graphene oxide derivatives via functionalization reaction with hexamethylene diisocyanate. *Nanomaterials* **2018**, *8*, 870.
[16] Tang, S. J.; Wang, H. M.; Wang, H. S.; Sun, Q. J.; Zhang, X. Y.; Cong, C. X.; Xie, H.; Liu, X. Y.; Zhou, X. H.; Huang, F. Q. et al. Silane-catalysed fast growth of large single-crystalline graphene on hexagonal boron nitride. *Nat. Commun.* **2015**, *6*, 6499.
[17] Panchal, V.; Yang, Y. F.; Cheng, G. J.; Hu, J. N.; Kruskopf, M.; Liu, C. I.; Rigosi, A. F.; Melios, C.; Walker, A. R. H.; Newell, D. B. et al. Confocal laser scanning microscopy for rapid optical characterization of graphene. *Commun. Phys.* **2018**, *1*, 83.
[18] Akhtar, F.; Dabrowski, J.; Lukose, R.; Wenger, C.; Lukosius, M. Chemical vapor deposition growth of graphene on 200 mm Ge(110)/Si wafers and *ab initio* analysis of differences in growth mechanisms on Ge(110) and Ge(001). *ACS Appl. Mater. Interfaces* **2023**, *15*, 36966–36974.
[19] Seo, D. H.; Pineda, S.; Woo, Y. C.; Xie, M.; Murdock, A. T.; Ang, E. Y. M.; Jiao, Y. L.; Park, M. J.; Lim, S. I.; Lawn, M. et al. Anti-fouling graphene-based membranes for effective water desalination. *Nat. Commun.* **2018**, *9*, 683.
[20] Thodkar, K.; Gramm, F. Enhanced mobility in suspended chemical vapor-deposited graphene field-effect devices in ambient conditions. *ACS Appl. Mater. Interfaces* **2023**, *15*, 37756–37763.
[21] Waduge, P.; Larkin, J.; Upmanyu, M.; Kar, S.; Wanunu, M. Programmed synthesis of freestanding graphene nanomembrane arrays. *Small* **2015**, *11*, 597–603.
[22] Chen, H. W.; Yang, Y. R.; Liu, Q.; Cui, M. F.; Chen, X.; Fei, Z. Y.; Tao, Z. L.; Wang, M. H.; Qiao, X. A citric acid-assisted deposition strategy to synthesize mesoporous SiO_2-confined highly dispersed $LaMnO_3$ perovskite nanoparticles for *n*-butylamine catalytic oxidation. *RSC Adv.* **2019**, *9*, 8454–8462.
[23] Sengar, S. K.; Mehta, B. R.; Kumar, R.; Singh, V. In-flight gas phase growth of metal/multi layer graphene core shell nanoparticles with controllable sizes. *Sci. Rep.* **2013**, *3*, 2814.
[24] Xie, M. S.; Luo, H. C.; Liu, X. J.; Yin, C. C. Development and challenge of coal-based nanocarbon materials and their application in water treatment: A review. *Discover Nano* **2024**, *19*, 162.
[25] Schaper, N.; Alameri, D.; Kim, Y.; Thomas, B.; McCormack, K.; Chan, M.; Divan, R.; Gosztola, D. J.; Liu, Y. Z.; Kuljanishvili, I. Controlled fabrication of quality ZnO NWs/CNTs and ZnO NWs/Gr heterostructures via direct two-step CVD method. *Nanomaterials* **2021**, *11*, 1836.
[26] Zhang, H.; Zhang, Y. G.; Li, J.; Ma, Z. N. Advantages of structure and electrochemical properties of graphene prepared from tectonically deformed coal. *ACS Omega* **2023**, *8*, 25142–25154.
[27] Rodríguez-Villanueva, S.; Mendoza, F.; Weiner, B. R.; Morell, G. Graphene film growth on silicon carbide by hot filament chemical vapor deposition. *Nanomaterials* **2022**, *12*, 3033.
[28] Shearer, C. J.; Slattery, A. D.; Stapleton, A. J.; Shapter, J. G.; Gibson, C. T. Accurate thickness measurement of graphene. *Nanotechnology* **2016**, *27*, 125704.
[29] Kresse, G.; Furthmüller, J. Efficiency of *ab-initio* total energy calculations for metals and semiconductors using a plane-wave basis set. *Comput. Mater. Sci.* **1996**, *6*, 15–50.
[30] Kresse, G.; Joubert, D. From ultrasoft pseudopotentials to the projector augmented-wave method. *Phys. Rev. B* **1999**, *59*, 1758–1775.
[31] Grimme, S.; Antony, J.; Ehrlich, S.; Krieg, H. A consistent and accurate *ab initio* parametrization of density functional dispersion correction (DFT-D) for the 94 elements H–Pu. *J. Chem. Phys.* **2010**, *132*, 154104.
[32] Li, L.; Liu, X. L.; Wang, G.; Liu, Y. L.; Kang, W. M.; Deng, N. P.; Zhuang, X. P.; Zhou, X. H. Research progress of ultrafine alumina fiber prepared by sol-gel method: A review. *Chem. Eng. J.* **2021**, *421*, 127744.
[33] Yuan, Q.; Yin, A. X.; Luo, C.; Sun, L. D.; Zhang, Y. W.; Duan, W. T.; Liu, H. C.; Yan, C. H. Facile synthesis for ordered mesoporous γ-aluminas with high thermal stability. *J. Am. Chem. Soc.* **2008**, *130*, 3465–3472.
[34] Chen, F. R.; Davis, J. G.; Fripiat, J. J. Aluminum coordination and Lewis acidity in transition aluminas. *J. Catal.* **1992**, *133*, 263–278.
[35] Seok, J.; Phan, N. T. Y.; Kim, J. C.; Shin, H.; Choi, M. Catalytic synergy between Lewis acidic alumina and Pt in hydrodechlorination for plastic chemical recycling. *J. Am. Chem. Soc.* **2024**, *146*, 23881–23890.
[36] Du, Z. P.; Wang, C. Y.; Zhang, R. H.; Wang, X. M.; Li, X. M. Applications of graphene and its derivatives in bone repair: Advantages for promoting bone formation and providing real-time detection, challenges and future prospects. *Int. J. Nanomedicine* **2020**, *15*, 7523–7551.
[37] Shamshirgar, A. S.; Hernández, R. E. R.; Tewari, G. C.; Ivanov, R.; Mikli, V.; Karppinen, M.; Hussainova, I. Layered structure of alumina/graphene-augmented-inorganic-nanofibers with directional electrical conductivity. *Carbon* **2020**, *167*, 634–645.
[38] Pitkänen, O.; Tolvanen, J.; Szenti, I.; Kukovecz, Á.; Hannu, J.; Jantunen, H.; Kordas, K. Lightweight hierarchical carbon nanocomposites with highly efficient and tunable electromagnetic interference shielding properties. *ACS Appl. Mater. Interfaces* **2019**, *11*, 19331–19338.
[39] Cheng, Y.; Li, X. Y.; Qin, Y. X.; Fang, Y. T.; Liu, G. L.; Wang, Z. Y.; Matz, J.; Dong, P.; Shen, J. F.; Ye, M. X. Hierarchically porous polyimide/$Ti_3C_2T_x$ film with stable electromagnetic interference shielding after resisting harsh conditions. *Sci. Adv.* **2021**, *7*, eabj1663.
[40] Mao, Q. Y.; Qiao, L.; Zheng, J. W.; Ying, Y.; Yu, J.; Li, W. C.; Che, S. L.; Cai, W. Injection molding and sintering of ZrO_2 ceramic powder modified by a zirconate coupling agent. *Materials* **2022**, *15*, 7014.
[41] Xiang, Z.; Shi, Y. Y.; Zhu, X. J.; Cai, L.; Lu, W. Flexible and waterproof 2D/1D/0D construction of MXene-based nanocomposites for electromagnetic wave absorption, EMI shielding, and photothermal conversion. *Nano-Micro Lett.* **2021**, *13*, 150.
[42] Wang, L.; Song, P.; Lin, C. T.; Kong, J.; Gu, J. W. 3D shapeable, superior electrically conductive cellulose nanofibers/$Ti_3C_2T_x$ MXene aerogels/epoxy nanocomposites for promising EMI shielding. *Research* **2020**, *2020*, 4093732.
[43] Liang, C. B.; Gu, Z. J.; Zhang, Y. L.; Ma, Z. L.; Qiu, H.; Gu, J. W. Structural design strategies of polymer matrix composites for electromagnetic interference shielding: A review. *Nano-Micro Lett.* **2021**, *13*, 181.
[44] Deng, Y. L.; Chen, Y. Q.; Liu, W.; Wu, L. L.; Wang, Z.; Xiao, D.; Meng, D. C.; Jiang, X. G.; Liu, J. R.; Zeng, Z. H. et al. Transparent electromagnetic interference shielding materials using MXene. *Carbon Energy* **2024**, *6*, e593.
[45] Chung, D. D. L. A perspective on electromagnetic interference shielding materials comprising exfoliated graphite. *Carbon* **2024**, *216*, 118569.
[46] Xia, Y. X.; Gao, W. W.; Gao, C. A review on graphene-based electromagnetic functional materials: Electromagnetic wave shielding and absorption. *Adv. Funct. Mater.* **2022**, *32*, 2204591.
[47] Liu, J.; Yu, M. Y.; Yu, Z. Z.; Nicolosi, V. Design and advanced manufacturing of electromagnetic interference shielding materials. *Mater. Today* **2023**, *66*, 245–272.
[48] Tian, J. H.; Xu, Y.; Yang, Y.; Zhao, Y. C.; Man, W.; Wang, J. G.

Research on residual-current measurement system of substation considering magnetic shielding effect. *Sensors* **2024**, *24*, 632.

[49] Kruželák, J.; Kvasničáková, A.; Hložeková, K.; Plavec, R.; Dosoudil, R.; Gořalík, M.; Vilčáková, J.; Hudec, I. Mechanical, thermal, electrical characteristics and EMI absorption shielding effectiveness of rubber composites based on ferrite and carbon fillers. *Polymers* **2021**, *13*, 2937.

[50] Sun, M. Y.; Wang, S.; Liang, Y. B.; Wang, C.; Zhang, Y. H.; Liu, H.; Zhang, Y.; Han, L. Flexible graphene field-effect transistors and their application in flexible biomedical sensing. *Nano-Micro Lett.* **2025**, *17*, 34.

[51] Askari, M. B.; Salarizadeh, P.; Veisi, P.; Samiei, E.; Saeidfirozeh, H.; Moghadam, M. T. T.; Di Bartolomeo, A. Transition-metal dichalcogenides in electrochemical batteries and solar cells. *Micromachines* **2023**, *14*, 691.

[52] Zheng, M. K.; Ma, X. G.; Hu, J. S.; Zhang, X. X.; Li, D.; Duan, W. Y. Novel recyclable BiOBr/Fe_3O_4/RGO composites with remarkable visible-light photocatalytic activity. *RSC Adv.* **2020**, *10*, 19961–19973.

[53] Shamshirgar, A. S.; Álvarez, M. F.; del Campo, A.; Fernández, J. F.; Hernández, R. E. R.; Ivanov, R.; Rosen, J.; Hussainova, I. Versatile graphene-alumina nanofibers for microwave absorption and EMI shielding. *Carbon* **2023**, *210*, 118057.

[54] Jia, W.; Zhou, L. R.; Jiang, M.; Du, J.; Zhang, M. Y.; Han, E. L.; Niu, H. Q.; Wu, D. Z. Fabrication of polyimide/graphene nanosheet composite fibers via microwave-assisted imidization strategy. *RSC Adv.* **2021**, *11*, 32647–32653.

[55] Song, H.; Kim, B. G.; Kim, Y. S.; Bae, Y. S.; Kim, J.; Yoo, Y. Synergistic effects of various ceramic fillers on thermally conductive polyimide composite films and their model predictions. *Polymers* **2019**, *11*, 484.

[56] Vasquez, S.; Angeli, M. A. C.; Polo, A.; Costantini, A.; Petrelli, M.; Avancini, E.; Di Cagno, R.; Gobbetti, M.; Gaiardo, A.; Valt, M. et al. *In vitro* gastrointestinal gas monitoring with carbon nanotube sensors. *Sci. Rep.* **2024**, *14*, 825.

[57] Lan, Z. X.; Li, C. Y.; Yu, Y. L.; Wei, J. Colorless semi-alicyclic copolyimides with high thermal stability and solubility. *Polymers* **2019**, *11*, 1319.

[58] Li, Y. H.; Zhu, Y. F.; Jiang, G. P.; Cano, Z. P.; Yang, J.; Wang, J.; Liu, J. L.; Chen, X. H.; Chen, Z. W. Boosting the heat dissipation performance of graphene/polyimide flexible carbon film via enhanced through-plane conductivity of 3D hybridized structure. *Small* **2020**, *16*, 1903315.

[59] Lee, C. C.; Shih, R. C.; Huang, P. C.; Tseng, S. F. Adhesion enhancement of conductive graphene/PI substrates through a vacuum plasma system. *Surf. Coat. Technol.* **2020**, *388*, 125601.

[60] Ma, L. R.; Wang, Y. X.; Wang, Y. Y.; Wang, C. G.; Gao, X. P. Graphene induced carbonization of polyimide films to prepared flexible carbon films with improving-thermal conductivity. *Ceram. Int.* **2020**, *46*, 3332–3338.